metals

MDPI

Article

Radiographic Visibility Limit of Pores in Metal Powder for Additive Manufacturing

Gerd-Rüdiger Jaenisch [1], Uwe Ewert [2], Anja Waske [1] and Alexander Funk [1,*]

[1] Bundesanstalt für Materialforschung und-prüfung (BAM), Unter den Eichen 87, D-12205 Berlin, Germany; gerd-ruediger.jaenisch@bam.de (G.-R.J.); anja.waske@bam.de (A.W.)
[2] KOWOTEST GmbH, Solinger Straße 186, D-40764 Langenfeld, Germany; uwe@ewert-net.de
* Correspondence: alexander.funk@bam.de; Tel.: +49-30-8104-3251

Received: 11 November 2020; Accepted: 30 November 2020; Published: 4 December 2020

Abstract: The quality of additively manufactured (AM) parts is determined by the applied process parameters used and the properties of the feedstock powder. The influence of inner gas pores in feedstock particles on the final AM product is a phenomenon which is difficult to investigate since very few non-destructive measurement techniques are accurate enough to resolve the micropores. 3D X-ray computed tomography (XCT) is increasingly applied during the process chain of AM parts as a non-destructive monitoring and quality control tool and it is able to detect most of the pores. However, XCT is time-consuming and limited to small amounts of feedstock powder, typically a few milligrams. The aim of the presented approach is to investigate digital radiography of AM feedstock particles as a simple and fast quality check with high throughput. 2D digital radiographs were simulated in order to predict the visibility of pores inside metallic particles for different pore and particle diameters. An experimental validation was performed. It was demonstrated numerically and experimentally that typical gas pores above a certain size (here: 3 to 4.4 µm for the selected X-ray setup), which could be found in metallic microparticles, were reliably detected by digital radiography.

Keywords: additive manufacturing; feedstock powder; porosity; radiography; digital detector array; numerical simulation; detectability

1. Introduction

The reliability of additively manufactured (AM) parts depends to a large degree on the defects and irregularities they contain [1]. Typical flaws in AM parts include delaminations, cracks, inclusions, and pores. For the laser powder bed fusion (LPBF) process, most defects are formed during the dynamic melting process, when the laser interacts with the solid and the melt pool [2,3]. The AM community distinguishes between lack of fusion pores, which are flat and irregular pores (voids) between non-fused powder layers, keyhole pores, which are irregular pores (voids) created by the laser and a high energy input, and gas pores, which are mostly spherical pores formed by adding gas to the melt pool [2,4–8]. A detailed review of pores and voids created during the AM build process was recently published by Sola et al. [2].

Another possible source for gas pores in AM parts is pores already present in the feedstock powder [6,9–12]. Due to the fast heating and cooling rate of the melt pool up to 10^6 K/s [13] during the LPBF process, gas pores in the powder become bubbles in the melt pool, which under certain circumstances do not have sufficient time to reach the surface of the melt by convection [2,14]. Hence, it is important to check the quality of the feedstock powders, for instance, by determining its overall porosity and pore size distribution [6,15,16]. However, determining the porosity of powders experimentally, e.g., by pycnometry or metallography, is a challenging task [16]. For standard AM materials like steels, aluminum, magnesium, titanium, and nickel alloys, typical porosities of the feedstock powder are

below 1 vol.% [10,16]. In particular, high feedstock powder porosities and single particles with large pores influence the melting behavior of the powder and are likely to merge and solidify together with the melt pool and may become a defect in the final part [2,6]. Several testing methods for the characterization of AM feedstock powders are standardized [17,18]. However, since currently no common quality requirements or certification for AM powders exist, there is the uncertainty that the quality of the powder might vary between different manufacturers and batches. This is particularly true for non-standard AM powder materials, for instance, functional materials like shape-memory alloys [19], permanent magnets [20], or magnetic refrigerants [21], that are now being adapted to AM. For non-standard powders, the production of the feedstock powder is particularly challenging, as the atomization parameters need to be optimized. Large overall porosities up to 24 vol.%, large pore sizes, and shape irregularities leading to a poor powder flowability are also reported for standard AM materials [6,9,12], which require quality control of every powder batch before using them for AM [1].

Feedstock powders for AM are usually checked for their size and shape distribution using sieve-based, light scattering, or direct imaging methods [15,22]. Since these rely on the outer contour of the geometry or optical imaging, internal defects of metal powders, like gas-filled pores, are not accessible. Very accurate determination of internal defects, as well as size and shape distributions of a powder, can be carried out using 3D X-ray computed tomography (XCT) [6,9,16,23]. However, the scan time for a typical powder sample with a commercial XCT device is rarely below one hour [16]. Depending on the size of the powder, the system magnification, and the detector size, only about 1000 to 1,000,000 particles can be imaged during one scan when the highest resolution is required, since the field of view of XCT is limited. This number of particles is equivalent to a few milligrams of metal powder. When considering that several hundred grams and up to several kilograms of powder are needed to manufacture AM parts, milligram samples are not representative for the evaluation of feedstock powder batches and hence for meaningful quality assurance. A technology capable of screening larger amounts of particles in a shorter time is needed for this task.

In-line digital radiography of products and goods is already used, e.g., in fine casting inspection in industry, weld inspections, the food industry, and for luggage inspection at airports [24]. Correspondingly, 2D X-ray inspection was developed for speed and high throughput. In this paper, the potential and requirements of digital radiography for the quality assurance of metal powder by detecting spherical gas-filled pores in metal particles are evaluated. Nowadays, commercially available laboratory XCT scanners are used for measurements, which are available in most AM laboratories worldwide to inspect the final parts produced. However, in the present article, instead of collecting projections from different angles of the powder sample for a reconstruction of a 3D tomographic dataset, 2D radiographs of single layers of the powder are used for inspection. In practice, this would later require that, e.g., a conveyor belt-like or particle stream apparatus is used for moving the particles into the inspection region, similar to the ones used in light scattering devices or direct imaging devices for powder, like a commercial Camsizer® (Microtrac Retsch GmbH, Haan, Germany) [22,25,26]. For the study presented here, a metal alloy is used, but the pore imaging principle applies to other materials, as well. In this paper, a criterion based on a minimal contrast to noise ratio and a basic spatial image resolution is applied, which must be fulfilled in order to detect pores of certain sizes in a metallic particle by digital radiography.

2. Materials and Methods

2.1. Experimental Sample Preparation

The tested spherical gas-atomized powder material is a MnFePSi-based alloy [27], with a nominal particle size range of diameters between 100 µm and 150 µm. Note, the particle size range for numerical simulations is broader (see Section 2.5). The experimentally investigated powder represents the geometrical constitution of powders used in AM processes [1]. Both a multi-particle and single-particle sample were radiographed. For sample preparation, one side of a double-sided adhesive tape was

placed on a polymer substrate to ensure mechanical stiffness, whereas the other side was covered with particles. The multi-particle sample was fixed on a sample rod.

After testing the multi-particle sample, a single particle containing several pores was identified and isolated from the multi-particle sample using a micro-manipulation tool, radiography, tomography, and light microscopy. The isolated particle was fixed again on a sample rod.

2.2. Experimental Acquisition of Radiographic Images and Tomograms

Radiographic images were acquired employing a commercial X-ray computed tomography (XCT) device, GE nanotom m 180, and using the image acquisition software datos|x 2.2 acquisition (Waygate Technologies (Baker Hughes Digital Solutions GmbH), Wunstorf, Germany) [28]. A set of radiographic projections, taken at discrete angular positions of the observed sample, served as input data for a subsequent volume reconstruction using the image reconstruction software datos|x 2.2 reconstruction (Waygate Technologies, Wunstorf, Germany) [28]. For the experiments, a phoenix|X-ray micro-focus tube (Waygate Technologies, Wunstorf, Germany) with a tungsten transmission target on a diamond window and a digital detector array (DDA) of type DXR500L (Waygate Technologies, Wunstorf, Germany) was used [28]. The X-ray radiation was not filtered at the source side in order to achieve the highest possible intensity. The X-ray tube can be operated in different operation modes, varying the size of the focal spot. For the selected tube current and acceleration voltage range, nominal spot size of f = 5 µm in mode 0 and f = 1.3 µm in mode 2 are provided. In this work, mode 2 was used.

Both samples, the multi-particle sample (a) and the single-particle sample (b), were imaged using similar X-ray system parameters, as summarized in Table 1. For sample size reasons, the source to object distance (SOD) and the source to detector distance (SDD) were chosen to be 3 mm/600 mm (a) and 2 mm/400 mm (b), respectively. As a result, the effective pixel size of the radiographs and the voxel size of the volume reconstruction are 0.5 µm. For the tomographic reconstruction, 1700 projections (a) and 800 projections (b) were recorded while rotating the sample. An acquisition time of about 45 min is required for medium image quality for sample (a). To improve the image quality of the XCT projections (noise reduction), a skip of two projections and a frame averaging of five projections on each angular position were selected, which prolonged the total acquisition time by a factor of seven to about 5 h.

Table 1. Summary of experiments and their image acquisition parameters.

Scan Identifier	Tube Mode	Voltage (kV)	Current (µA)	SOD (mm)	SDD (mm)	M	Pixel/Voxel Size (µm)	Frame Averaging	Skip	No. of Projections	Frame Time (s)
2D (a)	2	130	100	3	600	200	0.5	10	none	1	1.5
3D (a)	2	130	100	3	600	200	0.5	5	2	1700	1.5
2D (b)	2	130	100	2	400	200	0.5	10	none	1	10
3D (b)	2	130	100	2	400	200	0.5	5	2	800	10

For the analysis of 3D volumes and the particle and pore size distributions, as well as for visualization, Thermo Fisher Scientific Avizo 9.2 software (Waltham, MA, USA) [29] was applied. The used analysis approaches to detect particles and pores in volumetric datasets can be found in [16].

2.3. Prediction of Pore Detectability by Human Observers

The basics for detecting small holes in objects, examined by human observers using radiography, were published in [30]. Here, a minimal contrast to noise ratio $\mathrm{CNR}_{\mathrm{min}}$ is derived as a criterion to determine the detection limit of hole plate image quality indicators at a magnification of one, depending on the basic spatial resolution of the detector $\mathrm{SR}_{\mathrm{b}}^{\mathrm{detector}}$ and the hole diameter d_{hole} given by the equation:

$$\mathrm{CNR}_{\mathrm{min}} = \frac{10 \cdot \mathrm{SR}_{\mathrm{b}}^{\mathrm{detector}}}{d_{\mathrm{hole}}} \quad (1)$$

This concept was extended considering the magnification M, spot size f, and the pore geometry [31]

$$\mathrm{CNR}_{\mathrm{min}} = \frac{10}{M} \cdot \frac{2}{\pi d_{\mathrm{pore}}} \sqrt{((M-1)f)^2 + \left(2\mathrm{SR}_{\mathrm{b}}^{\mathrm{detector}}\right)^2} \quad (2)$$

with d_{pore}—pore diameter. Note, the equation is independent of the material tested.

2.4. Image Analysis of Radiographs Based on the Contrast to Noise Ratio

The digital image analysis was carried out using the software ISee! version 1.11.1 (BAM, Berlin, Germany) [32] for the measurement of the contrast to noise ratio (CNR) in simulated and measured radiographs. The profile was drawn over the center of the powder particle pore to measure the contrast in the radiograph (see Figure 1). The noise was measured in a region of interest in the free beam area. The procedure for the noise measurement implemented in ISee! is described in [33]. The resulting CNR was compared to the theoretical minimal required $\mathrm{CNR}_{\mathrm{min}}$ for pore detection (see Section 2.3). The pore is visible to human observers if the determined CNR exceeds $\mathrm{CNR}_{\mathrm{min}}$, as calculated by Equation (2).

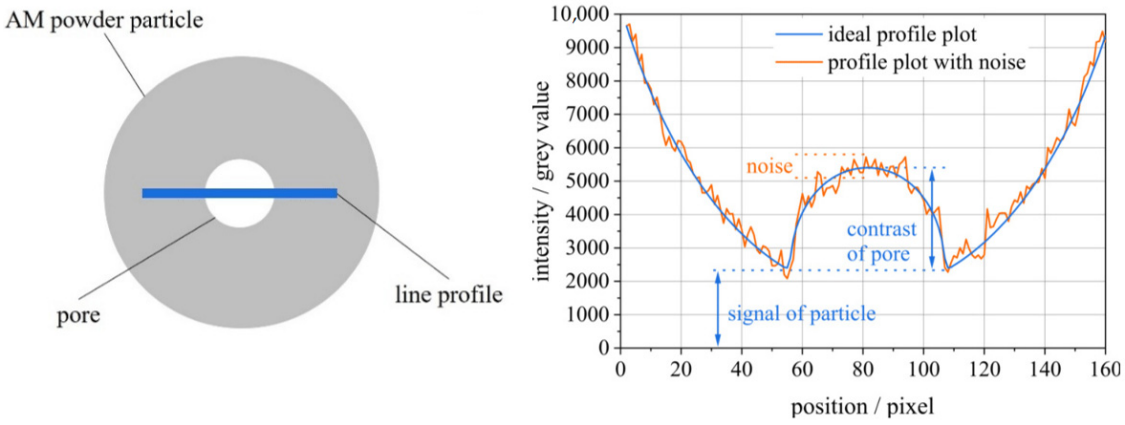

Figure 1. Scheme for measuring the contrast to noise ratio (CNR): the position of the line profile for the CNR measurement (**a**) and representation of the corresponding profile with and without noise to measure the CNR (**b**).

2.5. Numerical Simulation of Radiographic Images

The radiographic simulation software *aRTist* (BAM, Berlin, Germany) [34–36] was used to model different inspection scenes of the feedstock powders, using physical models for the production, interaction, and detection of X-rays. The graphical user interface of *aRTist* allows for setting up experimental scenes with different components like the radiation source, different detectors, and geometries of the object under investigation, as shown in Figure 2a. The software combines analytical and Monte Carlo methods to efficiently model the interaction of X-rays with matter. Hence, the way in which X-rays are absorbed and scattered in an object can be simulated and the resulting radiographic image at the detector can be calculated.

For simulation, mode 2 of the XCT scanner (see Section 2.2) with a nominal focal spot size of f = 1.3 µm was applied, together with an acceleration voltage of 130 kV and maximum gray values of $\mathrm{GV}_{\mathrm{max}}$ = 4200, in accordance with the available experiments, and $\mathrm{GV}_{\mathrm{max}}$ = 10,000 to examine the influence of the exposure time on the detectability of the pores.

The following parameters were used for the simulation with *aRTist*:

1. Source:
   - Tungsten transmission target with a thickness of 5 µm;
   - Diamond window with a thickness of 200 µm;
   - Focal spot size of $f = 1.3$ µm;
   - Tube voltage of 130 kV and spectrum resolution of 1 keV, no external filtering on tube side (for resulting spectrum, see Figure 2b).
2. Objects:
   - Powder particles: MnFePSi alloy, density of 6.4 g/cm^3;
   - Pores: air: N_2 0.755, O_2 0.231, Ar 0.013 (in mass percent), density of 0.001293 g/cm^3.
3. Detector:
   - Pixel size of 100 µm;
   - Basic spatial resolution of the detector: $SR_b^{detector} = 130$ µm;
   - Covered by a 750 µm thick carbon fiber-reinforced plastic plate;
   - Maximum gray value of (a) GV_{max} = 4200 and (b) GV_{max} = 10,000;
   - Internal scatter ratio of 15%, internal scatter ratio correlation length of 10 mm, gray response of 1000 GV/mGy, maximal signal-to-noise ratio (SNR) of 1400, efficiency of 500 $SNR_N/mGy^{1/2}$.
4. Geometry:
   - SDD = 400 mm;
   - SOD = 2 mm;
   - M = 200.

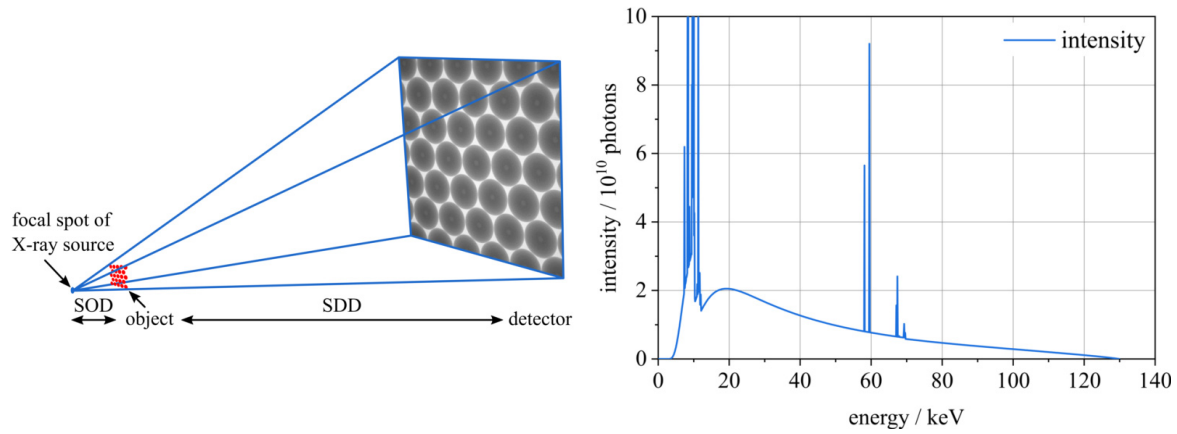

(**a**) (**b**)

Figure 2. Schematic representation of the radiographic setup with source, object, and detector in (**a**), and the 130 kV spectrum plot used in the simulation in (**b**).

For the numerical simulation, an idealized geometrical description was used to represent the feedstock particles in a size range between 10 µm and 150 µm, to cover the full range of commonly used AM feedstock powders [1]. The particles were assumed to be spherical and arranged in a single layer. The pores are described as spheres filled with air and positioned in the center of the powder particle, which yields the minimum achievable contrast in the radiographic images. Figure 3 shows an example of the geometric arrangement and the radiographic image of 441 particles with internal pores used for simulation. The high number of spheres was selected to permit a more accurate evaluation of

pore visibility. To determine the minimum detectable pore sizes, the actual pore diameter was reduced stepwise by 0.1 µm. Simulated radiographic images were analyzed after each step, as described in Section 2.4.

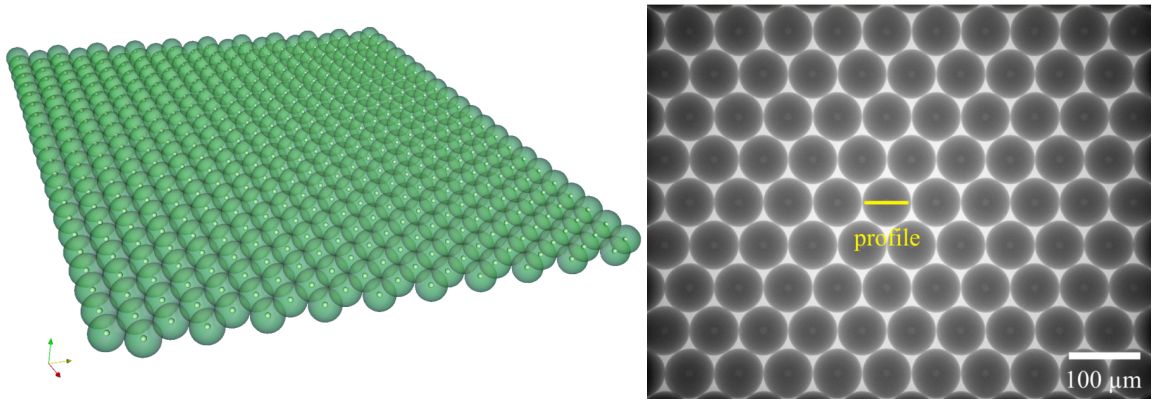

(**a**) (**b**)

Figure 3. Representation of a single layer of a 21 × 21 arrangement of metallic particles of 50 µm in diameter and with 5 µm air-filled pores inside, taken from the *aRTist* simulation scene (**a**). Radiographic image of the identical geometry with the profile (yellow inset) to investigate the visibility as function of CNR (**b**). The pores are the light gray areas in the center of the spheres.

3. Results and Discussion

3.1. Minimal Visible Pore Size

Figure 4 shows the CNR_{min} according to Equation (2) for two different focal spot sizes and $SR_b^{detector} = 130$ µm. For $f = 5$ µm (Figure 4a), the minimum required CNR_{min} is almost independent of the magnification in the selected range, while for $f = 1.3$ µm (Figure 4b) for small pores and micro- or nano-focus tubes, the CNR_{min} depends significantly on the magnification. Additionally, the CNR_{min} for $f = 5$ µm is generally higher than the smaller focal spot size of $f = 1.3$ µm, meaning that for a real experimental setup with known $SR_b^{detector}$ and proper exposure, small pores are more difficult to detect with a big focal spot size (Figure 4).

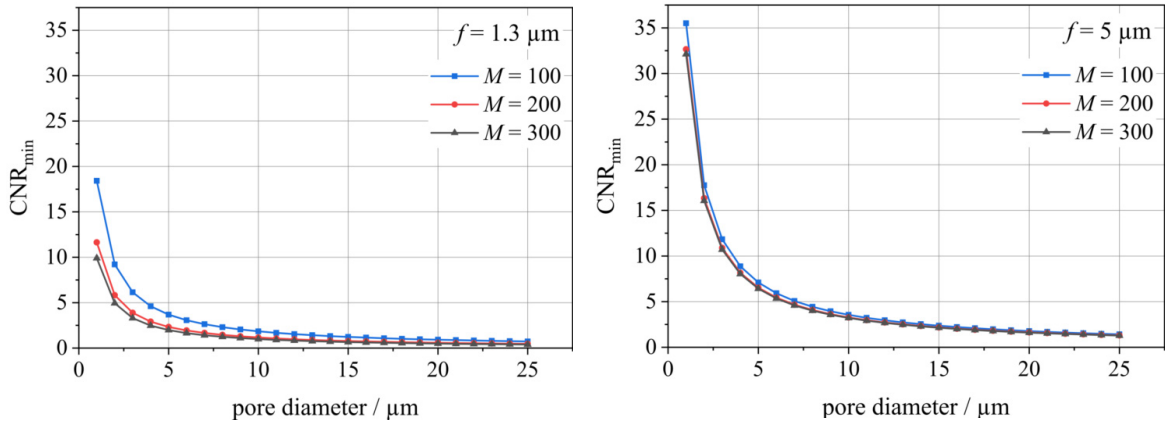

(**a**) (**b**)

Figure 4. Minimal contrast to noise ratio CNR_{min} for pore visibility according to Equation (2) with $SR_b^{detector} = 130$ µm, different magnifications M and the focal spot sizes: $f = 5$ µm (**a**) and $f = 1.3$ µm (**b**).

The diameter of a just visible pore, $d_{\text{pore\_min}}$, in a radiograph of spherical particles can be predicted as function of the radiographic setup and the exposure parameters as follows:

$$d_{\text{pore\_min}} = \frac{10}{M} \cdot \frac{2}{\pi \cdot \text{CNR}_{\text{min}}} \sqrt{((M-1)f)^2 + \left(2\text{SR}_{\text{b}}^{\text{detector}}\right)^2} \quad (3)$$

The magnification M, the focal spot size f, and the basic spatial detector resolution $\text{SR}_{\text{b}}^{\text{detector}}$ depend on the radiographic setup. The detectable pore size decreases if the focal spot size and the basic spatial resolution of the detector are selected to be as small as possible.

Furthermore, the detectable pore size also decreases if the CNR can be increased by the exposure conditions and M is optimized. The operator controls the pore contrast and noise by the selection of the X-ray energy and exposure parameters. The contrast is increased when the selected tube voltage is decreased. The CNR is increased if the noise is reduced. This requires increasing the tube current and the exposure time (for DDAs, increase frame time and frame averaging number). Generally, it is concluded that the CNR increases with the square root of exposure time and tube current. This requires an effective calibration of the digital detector array (DDA) to avoid an additional noise contribution by fixed pattern noise, which appears typically due to the sensitivity differences of the detector elements (pixels) and bad pixels. An increase in the tube voltage reduces the contrast and the noise, which influences the CNR depending on the attenuation process, typically the photo absorption or the Compton attenuation. At a higher tube voltage, where the Compton effect dominates, the contrast shows a low dependence on the selected tube voltage, but the exposure time is reduced significantly since the SNR increases proportionally to the tube voltage.

The ratio of particle diameter d_{particle} to pore diameter d_{pore}, referred to as DPP, influences the measured pore contrast slightly due to the measurement procedure, as shown in Figure 1. Figure 5 shows the surface curvature changes, as seen in the profile, if the DPP is changed from 2 to 10. The pore contrast is slightly reduced with decreasing DPP depending on the particle surface curvature and corresponding line profile change. For large particle diameters, compared to the pore diameters, the pore contrast does not change any more with increasing particle diameter.

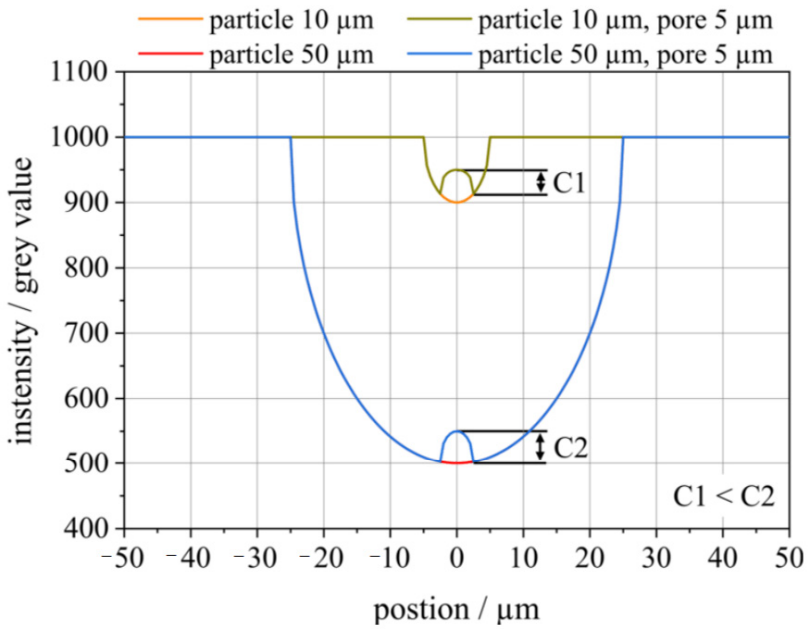

Figure 5. Contrast change as a function of the overlaid profiles of the pore and particle for different particle diameters. C1 is smaller than C2 for the same pore diameter, since the line profile of the larger particle (50 µm) is almost a flat plateau in contrast to the smaller particle.

A significant hardening of the spectrum is observed with increasing particle diameter for transmission microfocus tubes with diamond window and no prefiltering on the source side. Furthermore, the noise in the pore image increases due to the attenuation of larger particles. Consequently, the CNR is slightly reduced.

3.2. Simulation Results

By varying the size of the particles and the pores and determining whether the CNR of the pore signal in the radiographic image exceeds CNR_{min}, it can be determined whether a pore can be detected or not. The CNR_{min} value of Equation (2) as the visibility limit was verified by three operators for the simulated pores in the particles and accepted as a valid approach within a precision of about ±15% of the determined CNR, which was measured as shown in Figure 1 of the modeled images. In total, about 100 images were created and analyzed. As a result, the CNR_{min} obtained from Equation (2) was considered as valid limit by the three human observers. For the given simulation setup with $f = 1.3$ µm, a CNR_{min} for just visible pores of about 3, corresponding to pore diameters of about 4 µm, was determined. Bigger pores can be detected reliably, as the CNR will always exceed the CNR_{min}.

Based on this, Figure 6 shows the minimum pore size required in order to detect pores in metallic powder particles between 10 µm and 150 µm in diameter by means of digital radiography for the implemented X-ray setup. For the smallest particles with a diameter of 10 µm, the detectable pore diameter is equivalent to 35% of the particle diameter, while for the largest particles of 150 µm in diameter, the detectable pore has a diameter of 3% of the particle diameter (see Figure 6). The detectable minimum pore size increases slightly for very large and very small particles, with a local minimum at a particle diameter of about 70 µm. This is explained due to effects discussed in Section 3.1, e.g., the change of the X-ray spectrum (hardening) with increasing particle diameter on the right side of the graph in Figure 6 and the line profile shape (particle surface curvature), which yields a bias in the contrast measurement, for the left side of the graph in Figure 6.

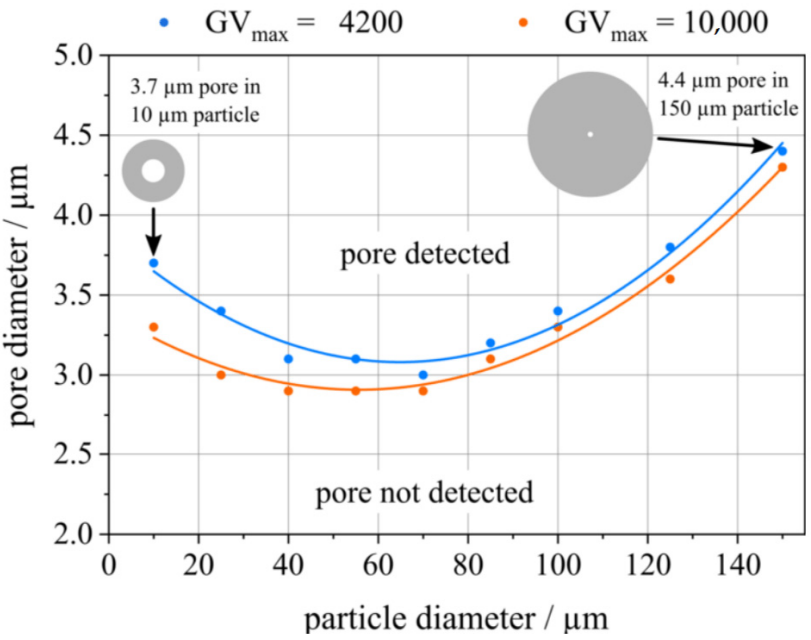

Figure 6. Diameter of the minimum pore sizes detectable by digital radiography in metal powder particles with diameters between 10 µm and 150 µm. The schematic insets are not to scale.

The minimum detectable pore sizes differ only slightly dependent on the selected exposure time of the detector with gray values of GV_{max} = 4200 and GV_{max} = 10,000 due to the limitation by the detector calibration (remaining detector fixed pattern noise) and internal backscatter in the detector (see Figure 6). The more highly illuminated image with GV_{max} = 10,000 demonstrates slightly smaller

detected pores. This indicates that experimental exposure parameters leading to GV_{max} = 4200 are sufficient to detect the smallest pores according to Equation (2) for the present X-ray setup ($SR_b^{detector}$, detector efficiency, magnification, focal spot size, and exposure parameters).

For GV_{max} = 4200, the smallest detectable pore sizes for three different particle diameters are summarized in Table 2, together with an additional example for a large particle with a large pore. The corresponding simulated images are shown in Figure 7. The additional example with a large pore is in accordance with a particle and pore size which are examined in the experimental results section (see Section 3.3).

Table 2. Detectable pore size diameters for different particle sizes (at a maximum gray value of GV_{max} = 4200).

Particle Diameter	Pore Diameter	CNR_{min}	Measured CNR
10 µm [1]	3.7 µm [1]	3.5	3.9
70 µm [1]	3.0 µm [1]	3.9	3.9
150 µm [1]	4.4 µm [1]	2.7	2.8
135 µm [2]	40 µm [2]	0.3	30.7

[1] Smallest detectable pore for the corresponding particle diameter. [2] Large pore and particle size, which was found in the experiment (see Section 3.3).

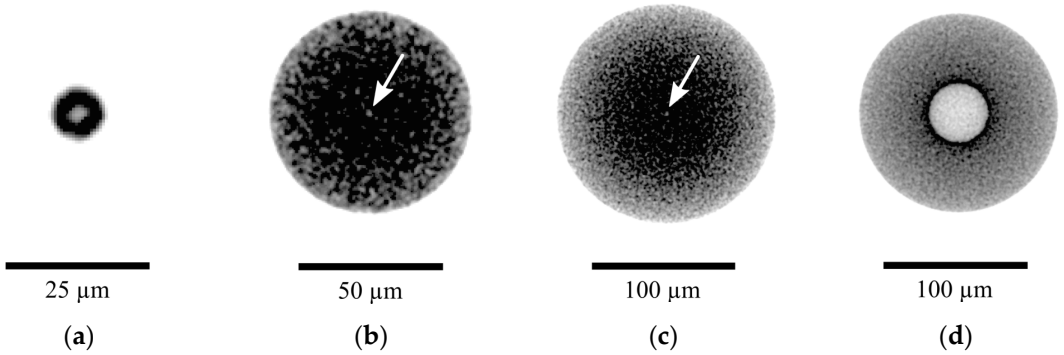

Figure 7. Simulated radiographs (GV_{max} = 4200) of different particle and pore diameters. The images were filtered, and the contrast was optimized for printed paper. (**a**–**c**) The smallest detectable pores for a particle diameter of (**a**) 10 µm, (**b**) 70 µm, and (**c**) 150 µm. Image (**d**) covers a particle diameter of 135 µm and a pore diameter of 40 µm, which is in the range of the particle and pore sizes found in the experiment (see Section 3.3). White arrows in (**b**,**c**) point to the centered pore. All images are in correspondence with the values listed in Table 2.

The smallest detectable pore sizes were found to be very similar in the range between 3.0 µm to 4.4 µm for the variety of particle sizes and GV_{max} = 4200. This can be explained by Equation (3) using a small focal spot size of $f = 1.3$ µm and a high magnification of M = 200 as well as the constant unsharpness of the system, which does not require the particle diameter.

Consequently, an almost constant pore diameter as a visibility limit, independent of the particle diameter, is expected. Due to the magnification of 200, the object's scattered radiation does not contribute to the image formation process. Therefore, only the attenuation differences in the materials (pores inside the powder particles) are essential for the contrast in the radiographic image. Basically, as it is measured here (Figure 1), the contrast can be approximated as proportional to the pore diameter, which applies to small pores. The noise is independent of the pore diameter, when measured in the free beam area. This approximation was applied since the noise could not be measured accurately behind the spheres and the noise changes only slightly for low contrast indications. The simulation did confirm that the visibility limit is just between 3.0 µm and 4.4 µm pore diameter for GV_{max} = 4200, for a sphere diameter range of 10 µm to 150 µm and for the selected setup.

It is shown in Figure 6 that the detectable pore size does vary by about a factor of 1.5 if the particle size varies by a factor of 15. The volume of a sphere increases with the third power of its diameter. Because of this geometrical relationship, the minimal detectable pore volume percentage of a particle of a certain size decreases significantly with the particle size. Figure 8 shows the previous results (Figure 6) on detectable pores expressed as the volume percent of the particles. For GV_{max} = 4200, it can be concluded that for the smallest powder particles of 10 µm, the smallest visible pore volume amounts to about 5.1 vol.%. For powder particles of 25 µm, the pore volume fraction decreases to 0.25 vol.% and, for the largest powder particles studied with a diameter of 150 µm, the detectable pore volume is equivalent to only 0.0025 vol.% of the particle volume. With increased exposure time and higher magnification, even smaller percentages of pore volume in relation to the particle volume can be detected.

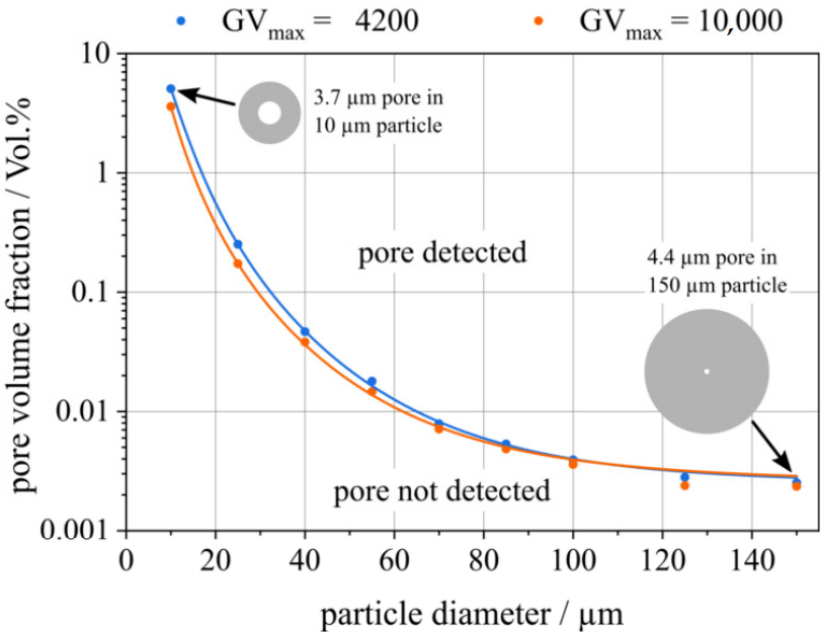

Figure 8. Minimum volume of pores detectable by digital radiography in metallic powder particles with diameters between 10 µm and 150 µm expressed as the pore volume fraction of the powder particles. The fraction of the detectable pore volume decreases rapidly with particle size. The schematic insets are not to scale.

This indicates that the contribution of the smallest detectable pore size in large powder particles to the overall porosity of the AM part is low and most likely does not affect the mechanical properties of the AM part. This is true if the volume fraction of the feedstock porosity is negligible and pore healing strategies in the AM fabrication process are applied [6,37]. A powder porosity of 5.1 vol.% is most likely critical for small particles with a diameter of 10 µm. The criticality of pore sizes in AM parts is discussed carefully in the literature, as many authors use very different materials, powder fractions, melting devices, and process parameters [1,2]. There is no strict rule for which amounts, sizes, and distributions of porosity in AM parts need to be avoided. In general, the porosity of an AM part should be as low as possible. However, it makes a difference if a single big pore or multiple very small pores create the total porosity of the AM part, as from mechanical testing it is known that the parts commonly crack at the biggest pores present [38]. Filigree and delicate AM parts, e.g., lattice structures, are especially endangered [26]. Whether a certain pore size or defect distribution is critical or not may also depend on the material, heat treatment, number of defects, arrangement of defects, location of the pores (close to surface or not), part geometry, and mechanical load. Most likely, very small pores and low total porosities are assumed to not be harmful. However, most potential harmful powder pores and large total feedstock porosities, e.g., hollow spheres or multiple medium-sized pores, can be

detected by radiography for the examined particle diameters. Hence, it can be concluded that digital radiography can reliably detect the important pores (in particles with diameters ranging from 10 µm to 150 µm), which potentially have an impact on the AM product.

3.3. Experimental Results and Comparison to Simulation

Figure 9a shows a radiograph and Figure 9b a tomogram of the multi-particle monolayer-like sample. The tomogram is used here as a basic information standard. From the images, it is obvious that the radiograph already contains most information of the powder particles, e.g., the diameters, positions, and shapes of the particles (gray regions), as well as the diameters, positions, and shapes of the pores (light gray regions). This is due to the prepared monolayer-like sample, which is optimized for 2D radiography. Most of the particles are located individually. However, in the experiment, it is difficult to prepare an exact monolayer of powder particles, and hence overlapping of particles may be observed, leading to dark gray regions. The particles are not ideally arranged and do not cover the complete detector area. Therefore, the maximum possible number of particles per image is not reached. Small satellites attached to the surfaces of the particles are visible, which originate from the atomization process. The shape of several particles deviates from a sphere and they form ellipsoidal-shaped particles. The imaged sample region contains about 70 particles in the size range of about 100 µm to 150 µm known from the 3D volume analysis. Pores of very different sizes are frequently observed in this powder sample specimen, which enhances the chance to find very small pores in this sample. Even multiple pores located in one particle are visible if they do not overlap significantly. The smallest visible pore diameter found in the radiographic image (see Figure 9a) is about 10 µm. The biggest visible pore diameters are about 80 µm. Pores with a diameter above 10 µm are directly visible without any image contrast optimization, as they show a large CNR, which is discussed in detail later. Smaller pores are more difficult to detect in big particles by human observers, as the total contrast and CNR of a small pore is low, which was described earlier (see Section 3.1, Figure 5). The detection of very small pores is difficult, as there is only one sample orientation imaged. The overlap of particles and pores present here disturbs the analysis. This applies even if the exact position of the pores is known from the tomogram (see Figure 9b). Therefore, a single particle was investigated in more detail (see Figure 10 and red arrows in Figure 9). In particular, here, a higher exposure time of the detector, leading to GV_{max} = 4200, was used.

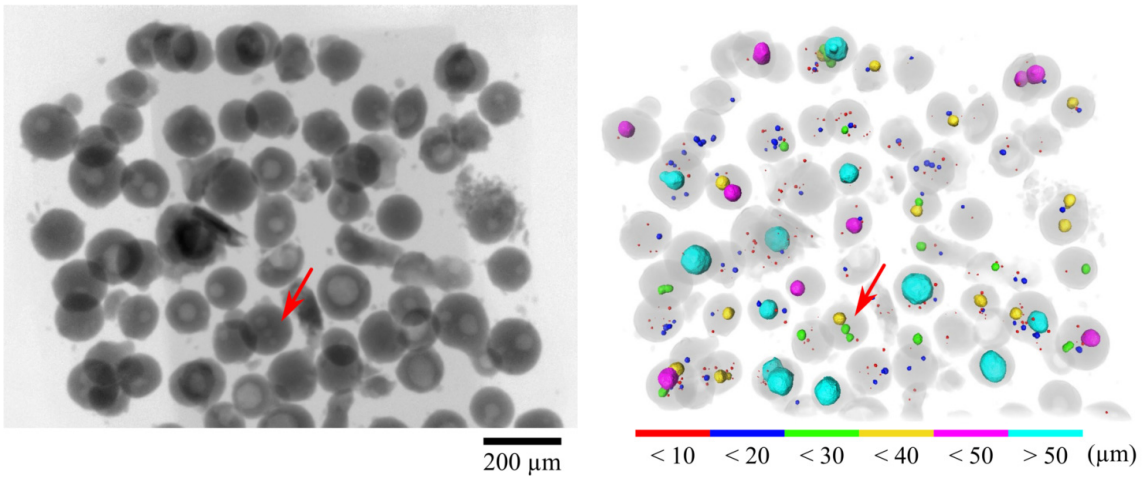

(**a**) (**b**)

Figure 9. Experimental verification of the simulation results. A monolayer-like multi-particle sample with diameters in between 100 µm and 150 µm and severe porosity inside was prepared and analyzed: (**a**) radiography and (**b**) rendering of the tomogram. A single particle from this monolayer-like sample was picked (red arrows) and was investigated in more detail (see Figure 10).

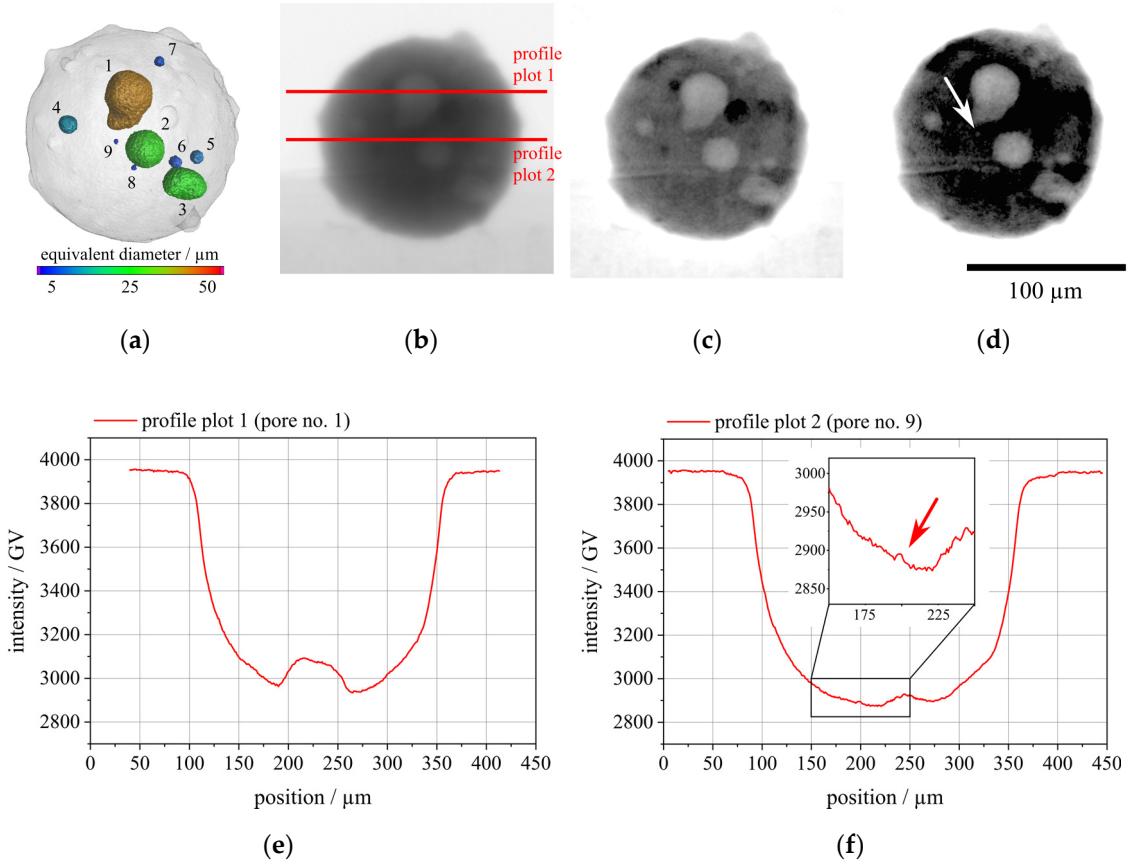

Figure 10. A rendered tomographic image and one radiographic projection of the single-particle sample with nine pores are shown in (**a**) and (**b**), respectively. In (**a**), the pores are numbered in correspondence to the index of the pores in Table 3. The contrast and brightness of (**b**) were enhanced based on filtering and a histogram correction, as presented in (**c**,**d**). In image (**b**), two red lines mark the profiles which belong to big pore no. 1 (**e**) and small pore no. 9 (**f**), respectively. Small pore no. 9 is highlighted by an arrow in (**d**,**f**).

Table 3. Measured CNR of pores in the single-particle sample.

Pore ID	Pore Equivalent Diameter XCT (µm)	Pore Diameter Radiography (µm)	CNR from Radiography
1	44	37	30
2	29	26	20
3	29	23	13.2
4	14	14	10
5	11	12	8
6	8	8	6.2
7	8	7	5.5
8	5	Not detected [1]	Not detected [1]
9	4	4	2.5

[1] Pore no. 8 was detected in the tomogram, but not in the radiograph, since it was overlapped by pore no. 2 at the selected projection angle (see Figure 10a).

The single particle covers an equivalent diameter of 137 µm. The equivalent diameter of an irregular shaped volume object (pore, particle) is the diameter of a perfect sphere of equivalent volume [39,40]. From the tomogram of the single-particle sample (Figure 10a), it is known that nine individual pores of different sizes are present (see Table 3). However, to detect all pores in the

radiographic image, one must turn the particle to its optimal projection direction to ensure the projected pores are visible separately. From different projection angles, the CNR was measured for the nine pores (Table 3) when the contrast sensitivity was optimal for the observer. Two-line profile plots of a big (profile plot 1) and a small (profile plot 2) pore are shown exemplarily together with radiographic images in Figure 10b–f. The contrast of the radiographs was optimized and filtered for the observed regions in Figure 10b,d to enhance the visibility on printed paper. Larger pores above 10 µm in diameter show a CNR above 8, whereas small pores down to 4 µm in diameter are close to the detectability limit of CNR_{min} according to Equation (2) (see Section 2.3). In some cases, the determined pore diameters from the radiography were found to be slightly smaller than the calculated volume equivalent pore diameters [39,40] from the corresponding tomogram. This can be explained by the orientation of irregularly shaped pores in the 2D projection and the usage of an equivalent pore diameter from the 3D analysis.

The presented numerical simulations show that it is feasible to detect pores down to a diameter of 3.0 µm to 4.4 µm in metallic microparticles of 10 µm to 150 µm in diameter by radiographic imaging, depending on the exposure parameters and the available setup (see Section 2.5). When comparing the experimental and simulated results, it is obvious that the numerical model is an idealized approximation of centered pores but gives valuable estimates of the detectable pore sizes. In practice, an optimal projection direction is important to identify individual pores if multiple pores per particle occur. In addition, pores are rarely placed exactly in the center of a particle. Pores located out of the center and close to the surface tend to be more difficult to detect, as they are placed within a strong signal gradient originating from the particle shape. Real feedstock powders may show satellites, irregular shapes, rough surfaces, or irregularly shaped pores, which have an orientation that is not known in any case when doing radiography. This potentially modifies the detectability. The low CNR of small pores occurring in the experiment may also originate from a variation of the device parameters. According to Equation (2), this would influence the required CNR_{min} to detect a pore of a certain size and may explain the difficulties to find pores close to the detectability limit in the experimental radiographs. The smallest detectable pores have a diameter of 4 µm and a CNR of about 2.5 (see Table 3), and therefore the simulated results are confirmed by the experiment within the measurement precision. As mentioned before, small pores in large particles have a negligible contribution to the total porosity of the final AM part. In contrast, large pores with a significant impact on the AM process are detected reliably.

In a final step, the pore size distribution of the metallic particles found experimentally by means of XCT (see Figure 9b) and 3D image analysis was compared with the visibility limit calculated by the simulation. Figure 11 shows the histogram of all equivalent pore diameters found in the multi-particle sample. The theoretical visibility limit from the simulation was found to be 3.0 µm to 4.4 µm for the used device and exposure conditions and is indicated as a red line. It is concluded from Figure 11 that more than 99 vol.% of the pore volume present in this powder sample can be detected using digital radiography within the 95% confidence bound.

3.4. The Potential of Digital Radiography in Comparison to Other Methods for Powder Analysis

AM powders are usually characterized by their shape and size distribution using methods like sieving, laser diffraction, or light microscopy (Camsizer® [22,25]) methods. However, as highlighted in this article, the investigation of internal powder defects, e.g., pores, is not necessarily in the scope of standard investigations. However, the density of a powder is an independent quality characteristic. To access the density or the pore size distribution of a powder, typically pycnometry, metallography, or XCT are used.

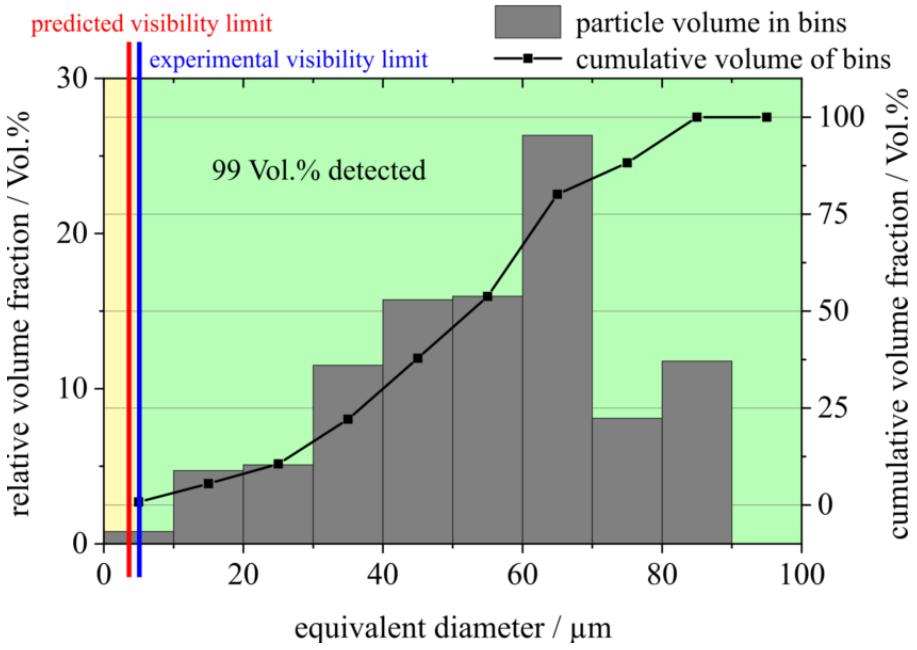

Figure 11. Histogram of the pore size distribution found in the metal powder by means of 3D X-ray computed tomography (XCT). Digital radiography was able to detect pores down to about 5 µm considering the 95% confidence bound at the selected setup (blue line). The predicted value for centered pores is 3 µm to 4.4 µm (red line). More than 99 vol.% of the pores volume present in this sample were detected experimentally.

All of the named methods have their benefits and drawbacks. An AM powder customized radiography technique comprises the potential to combine the best benefits of the discussed methods while minimizing the drawbacks. Sieving, laser diffraction, and light microscopy methods can screen large amounts of powder in a short time, but internal defects are not accessible. Pycnometry can also characterize large quantities of powder for its density, but not for its pore size distribution. Metallography or XCT can investigate the density and pore size distribution simultaneously. Still, both methods screen only small amounts of powder and need special attention, e.g., sample preparation or image analysis. For metallography, the sample preparation including polymer embedding, grinding, and polishing, is time-consuming. In addition, the imaging and image analysis takes time. When metallography is compared to high resolution XCT, it potentially investigates more particles, since XCT is a volume-based method and its quality of information can be treated as a "gold standard" for AM powders. However, XCT is a time-consuming method as well, including an optimal sample preparation, scanning, reconstruction, and image analysis. High throughputs of large powder batches are difficult to achieve by means of XCT.

As XCT takes projections from various angles of a sample, the data basis for the reconstructed volume and correspondingly the information content of internal sample features are much larger compared to digital radiography. However, considering the important information for AM powders, that pores are present or not, and that the actual position of the pores is not relevant per se, a radiographic imaging setup should be sufficient. The particle throughput of a radiographic setup compared to XCT is larger, even when radiography and XCT employ the same X-ray device setup. XCT needs a set of hundreds of projections from the sample for one scan. At the same time, radiography can image more particles. This is due to a geometrical relationship between the powder particle sizes and the X-ray device detector. One XCT scan can cover a cylindrical sample full of particles fitting the detector size. Imaging monolayer-like arranged powder particles fitting the complete detector by radiography leads to a larger throughput, when the XCT scan time or the amount of XCT projections is used as a time equivalent. The radiographic setup needs to be optimized for throughput, sensitivity, and resolution.

Therefore, digital radiography potentially combines the benefits of the methods, e.g., a high throughput and detailed internal powder information (pores). Drawbacks exist, as a complex sample preparation and image analysis need to be replaced by an automatic powder supply apparatus and dynamic and automated image analysis software, respectively, similar to the already employed techniques in light imaging and laser diffraction methods.

4. Summary and Outlook

The potential of digital radiography for the quality control of metal feedstock powders for AM in comparison to XCT was investigated in this work. It was shown numerically that for AM feedstock powder particles in the size range of 10 µm to 150 µm, pores down to 3.0 µm to 4.4 µm can be detected by X-ray radiography for the used commercial device in a typical setup and relevant exposure conditions. In most cases, the detectable pore size is sufficient for a quality control of the AM powder before it is processed. The numerical results were confirmed by the experiments. However, the selected X-ray setup is essential to detect smallest pores in particles. It can be improved by using a smaller focal spot size, higher magnification, longer exposure time, and a detector with smaller inherent detector unsharpness (lower $SR_b^{detector}$ value). Experimentally, it turned out that the orientation of the particles and pores relative to the radiographic projection direction influences the detectability, e.g., when pores or particles overlap in the radiograph. The minimal detectable pore volume amounts to around 5.1 vol.% of the particle volume for the smallest particle size studied in this work (10 µm). For the largest particle size (150 µm), this value decreases down to 0.0025 vol.%. Relevant particle pores, e.g., pores with a large pore to particle diameter ratio or large total feedstock powder porosities (multiple pores), with a potential negative impact on the AM process, are detected with high reliability by digital radiography.

As an outlook, an advanced digital radiography device can be designed to detect pores in AM powders. The powder would need to be moved on a conveyor belt or in a free-falling setup in order to achieve a high throughput. In addition, to speed up the imaging process, short exposure times are required, which can be achieved by faster and more efficient detectors and X-ray sources with high power and small focal spots, e.g., flash tubes. Such an advanced radiographic imaging setup would outrange competitive techniques and enable the opportunity to become a standard route for the quality assurance of AM powders.

Author Contributions: Conceptualization, G.-R.J. and A.W.; methodology, G.-R.J., A.F., and U.E.; software, G.-R.J., and A.F.; validation, G.-R.J., A.F., and U.E.; formal analysis, G.-R.J., A.F., and U.E.; investigation, G.-R.J., A.F., and U.E.; resources, A.W.; data curation, G.-R.J., A.F., and U.E.; writing—original draft preparation, G.-R.J., A.F., U.E., and A.W.; writing—review and editing, G.-R.J., A.F., U.E., and A.W.; visualization, G.-R.J., A.F., and U.E.; supervision, A.W.; project administration, A.W.; funding acquisition, none. All authors have read and agreed to the published version of the manuscript.

Funding: This research received no external funding.

Acknowledgments: The authors gratefully thank Uwe Zscherpel, Jörg Beckmann, David Schumacher, Alexander Ulbricht, Lina Pavasaryte, and Tobias Gustmann for fruitful discussions and proofreading of the manuscript. BASF is acknowledged for providing testing material.

Conflicts of Interest: The authors declare no conflict of interest.

References

1. Vock, S.; Klöden, B.; Kirchner, A.; Weißgärber, T.; Kieback, B. Powders for powder bed fusion: A review. *Prog. Addit. Manuf.* **2019**, *4*, 383–397. [CrossRef]
2. Sola, A.; Nouri, A. Microstructural porosity in additive manufacturing: The formation and detection of pores in metal parts fabricated by powder bed fusion. *J. Adv. Manuf. Process.* **2019**, *1*, 1. [CrossRef]
3. Martin, A.A.; Calta, N.P.; Khairallah, S.A.; Wang, J.; Depond, P.J.; Fong, A.Y.; Thampy, V.; Guss, G.M.; Kiss, A.M.; Stone, K.H.; et al. Dynamics of pore formation during laser powder bed fusion additive manufacturing. *Nat. Commun.* **2019**, *10*, 1987. [CrossRef] [PubMed]

4. Sinclair, L.; Leung, C.L.A.; Marussi, S.; Clark, S.J.; Chen, Y.; Olbinado, M.P.; Rack, A.; Gardy, J.; Baxter, G.J.; Lee, P.D. In situ radiographic and ex situ tomographic analysis of pore interactions during multilayer builds in laser powder bed fusion. *Addit. Manuf.* **2020**, *36*, 101512. [CrossRef]
5. Gould, B.; Wolff, S.; Parab, N.; Zhao, C.; Lorenzo-Martin, M.C.; Fezzaa, K.; Greco, A.; Sun, T. In Situ Analysis of Laser Powder Bed Fusion Using Simultaneous High-Speed Infrared and X-ray Imaging. *JOM* **2020**, 1–11. [CrossRef]
6. Cunningham, R.; Nicolas, A.; Madsen, J.; Fodran, E.; Anagnostou, E.; Sangid, M.D.; Rollett, A.D. Analyzing the effects of powder and post-processing on porosity and properties of electron beam melted Ti-6Al-4V. *Mater. Res. Lett.* **2017**, *5*, 516–525. [CrossRef]
7. Cunningham, R.; Zhao, C.; Parab, N.; Kantzos, C.; Pauza, J.; Fezzaa, K.; Sun, T.; Rollett, A.D. Keyhole threshold and morphology in laser melting revealed by ultrahigh-speed X-ray imaging. *Science* **2019**, *363*, 849–852. [CrossRef]
8. Hojjatzadeh, S.M.H.; Parab, N.; Guo, Q.; Qu, M.; Mohammad, S.; Hojjatzadeh, H.; Parab, N.D.; Xiong, L.; Zhao, C.; Escano, L.I.; et al. Direct observation of pore formation mechanisms during LPBF additive manufacturing process and high energy density laser welding. *Int. J. Mach. Tools Manuf.* **2020**, *153*, 103555. [CrossRef]
9. Ahsan, M.N.; Bradley, R.; Pinkerton, A.J. Microcomputed tomography analysis of intralayer porosity generation in laser direct metal deposition and its causes. *J. Laser Appl.* **2011**, *23*, 022009. [CrossRef]
10. Choo, H.; Sham, K.L.; Bohling, J.; Ngo, A.; Xiao, X.; Ren, Y.; Depond, P.J.; Matthews, M.J.; Garlea, E. Effect of laser power on defect, texture, and microstructure of a laser powder bed fusion processed 316L stainless steel. *Mater. Des.* **2019**, *164*, 107534. [CrossRef]
11. Morrow, B.M.; Lienert, T.J.; Knapp, C.M.; Sutton, J.O.; Brand, M.J.; Pacheco, R.M.; Livescu, V.; Carpenter, J.S.; Gray, G.T., III. Impact of Defects in Powder Feedstock Materials on Microstructure of 304L and 316L Stainless Steel Produced by Additive Manufacturing. *Metall. Mater. Trans. A* **2018**, *49*, 3637–3650. [CrossRef]
12. Sun, P.; Fang, Z.Z.; Zhang, Y.; Xia, Y. Review of the Methods for Production of Spherical Ti and Ti Alloy Powder. *JOM* **2017**, *69*, 1853–1860. [CrossRef]
13. Hooper, P.A. Melt pool temperature and cooling rates in laser powder bed fusion. *Addit. Manuf.* **2018**, *22*, 548–559. [CrossRef]
14. Leung, C.L.A.; Marussi, S.; Atwood, R.C.; Towrie, M.; Withers, P.J.; Lee, P.D. In situ X-ray imaging of defect and molten pool dynamics in laser additive manufacturing. *Nat. Commun.* **2018**, *9*, 1355. [CrossRef] [PubMed]
15. Slotwinski, J.A.; Garboczi, E.J.; Stutzman, P.E.; Ferraris, C.F.; Watson, S.S.; Peltz, M.A. Characterization of Metal Powders Used for Additive Manufacturing. *J. Res. Natl. Inst. Stand. Technol.* **2014**, *119*, 460–493. [CrossRef] [PubMed]
16. Heim, K.; Bernier, F.; Pelletier, R.; Lefebvre, L.P. High resolution pore size analysis in metallic powders by X-ray tomography. *Case Stud. Nondestruct. Test. Eval.* **2016**, *6*, 45–52. [CrossRef]
17. ISO. *ISO/ASTM 52907:2019-11—Additive Manufacturing—Feedstock Materials—Methods to Characterize Metal Powders*; ISO: Geneva, Switzerland, 2019.
18. ASTM. *ASTM F3049-14—Standard Guide for Characterizing Properties of Metal Powders Used for Additive Manufacturing Processes*; ASTM: West Conshohocken, PA, USA, 2014.
19. Gustmann, T.; dos Santos, J.M.; Gargarella, P.; Kühn, U.; Van Humbeeck, J.; Pauly, S. Properties of Cu-Based Shape-Memory Alloys Prepared by Selective Laser Melting. *Shape Mem. Superelast.* **2016**, *3*, 24–36. [CrossRef]
20. Kolb, T.; Huber, F.; Akbulut, B.; Donocik, C.; Urban, N.; Maurer, D.; Franke, J. Laser Beam Melting of NdFeB for the production of rare-earth magnets. In Proceedings of the 2016 6th International Electric Drives Production Conference (EDPC), Nuremberg, Germany, 30 November–1 December 2016; pp. 34–40. [CrossRef]
21. Kagathara, J.; Wieland, S.; Gärtner, E.; Uhlenwinkel, V.; Steinbacher, M. Heat Treatment and Formation of Magnetocaloric 1:13 Phase in $LaFe_{11.4}Si_{1.2}Co_{0.4}$ Processed by Laser Beam Melting. *Materials* **2020**, *13*, 773. [CrossRef]
22. Westermann, J.; Raatz, G. Improving quality control through effective particle characterisation of metal powders. *Powder Metall. Rev.* **2016**, *5*, 95–99. Available online: www.pm-review.com (accessed on 15 October 2020).

23. Thiede, T.; Mishurova, T.; Evsevleev, S.; Serrano-Munoz, I.; Gollwitzer, C.; Bruno, G. 3D Shape Analysis of Powder for Laser Beam Melting by Synchrotron X-ray CT. *Quantum Beam Sci.* **2019**, *3*, 3. [CrossRef]
24. Russo, P. (Ed.) *Handbook of X-ray Imaging: Physics and Technology*, 1st ed.; Series in Medical Physics and Biomedical Engineering; CRC Press Taylor & Francis Group: Boca Raton, FL, USA, 2018; ISBN 9781498741521.
25. Camsizer Website. Microtrac Retsch GmbH: Haan, Germany. Available online: www.microtrac.de (accessed on 15 October 2020).
26. Gustmann, T.; Gutmann, F.; Wenz, F.; Koch, P.; Stelzer, R.; Drossel, W.G.; Korn, H. Properties of a superelastic NiTi shape memory alloy using laser powder bed fusion and adaptive scanning strategies. *Prog. Addit. Manuf.* **2020**, *5*, 11–18. [CrossRef]
27. Miao, X.; Wang, W.; Liang, H.; Qian, F.; Cong, M.; Zhang, Y.; Muhammad, A.; Tian, Z.; Xu, F. Printing $(Mn,Fe)_2(P,Si)$ magnetocaloric alloys for magnetic refrigeration applications. *J. Mater. Sci.* **2020**, *55*, 6660–6668. [CrossRef]
28. Waygate Technologies Website. Waygate Technologies (Baker Hughes Digital Solutions GmbH): Wunstorf, Germany. Available online: www.bakerhughesds.com (accessed on 15 October 2020).
29. Thermo Fischer Scientific Avizo Software Website. Thermo Fischer Scientific Inc.: Waltham, MA, USA. Available online: www.thermofisher.com (accessed on 15 October 2020).
30. Ewert, U.; Zscherpel, U.; Heyne, K.; Jechow, M.; Bavendiek, K. Image quality in digital industrial radiology. *Mater. Eval.* **2012**, *70*, 955–964.
31. Jaenisch, G.-R.; Ewert, U. On the radiographic detectability of pores in spherically shaped matter by digital detector arrays. *Nucl. Instrum. Methods Phys. Res. Sec. A* **2021**, submitted.
32. ISee! Software Website. BAM: Berlin, Germany. Available online: http://www.zscherpel.info/ic/ (accessed on 15 October 2020).
33. ASTM. *ASTM E2446-16—Standard Practice for Manufacturing Characterization of Computed Radiography Systems*; ASTM: West Conshohocken, PA, USA, 2014.
34. Bellon, C.; Deresch, A.; Gollwitzer, C.; Jaenisch, G.-R. Radiographic Simulator *aRTist*: Version 2. In Proceedings of the 18th World Conference on Nondestructive Testing, Durban, South Africa, 16–20 April 2012.
35. Bellon, C.; Jaenisch, G.-R. *aRTist*—Analytical RT Inspection Simulation Tool. In Proceedings of the International Symposium on Digital Industrial Radiology and Computed Tomography DIR 2007, Lyon, France, 25–27 June 2007.
36. aRTist Software Website. BAM: Berlin, Germany. Available online: www.aRTist.bam.de (accessed on 15 October 2020).
37. Gustmann, T.; Schwab, H.; Kühn, U.; Pauly, S. Selective laser remelting of an additively manufactured Cu-Al-Ni-Mn shape-memory alloy. *Mater. Des.* **2018**, *153*, 129–138. [CrossRef]
38. Du Plessis, A.; Yadroitsava, I.; Yadroitsev, I. Effects of defects on mechanical properties in metal additive manufacturing: A review focusing on X-ray tomography insights. *Mater. Des.* **2020**, *187*, 108385. [CrossRef]
39. Jennings, B.R.; Parslow, K. Particle Size Measurement: The Equivalent Spherical Diameter. *Proc. R. Soc. Lond. A* **1988**, *419*, 137–149. [CrossRef]
40. DIN. *DIN ISO 9276-6:2012-01—Darstellung der Ergebnisse von Partikelgrößenanalysen—Teil 6: Deskriptive und quantitative Darstellung der Form und Morphologie von Partikeln*; DIN: Berlin, Germany, 2012.